SSRG International Journal of Electrical and Electronics Engineering
ISSN: 2348-8379/ https://doi.org/10.14445/23488379/IJEEE-V13I2P115

Volume 13 Issue 2, 182-197, February 2026
© 2026 Seventh Sense Research Group®

Original Article

An Intelligent ANN-Controlled Grid-Connected Solar PV System with Improved Stability for Multi-Application Energy Management

J. Srinu Naick[1], D.Srinivasarao[2], D. Nageswara Rao[3,] K. Chandrashekar[4], M. Naresh[5], Ch. Rambabu[6],
K. Hari Krishna[7]

[1]*Department of Electrical and Electronics Engineering, Chadalawada Ramanamma Engineering College, Andhra Pradesh, India.*
[2]*Department of Electrical and Electronics Engineering, Universal Engineering College, Andhra Pradesh, India.*
[3,4,5]*Department of Electrical and Electronics Engineering, Malla Reddy College of Engineering & Technology, Telangana, India.*
[6]*Department of Electrical and Electronics Engineering, Vasireddy Venkatadri Institute of Technology, Andhra Pradesh, India.*
[7]*Department of Electrical and Electronics Engineering, Kallam Haranadhareddy Institute of Technology, Andhra Pradesh, India.*

[1]*Corresponding Author : speaksrinu@gmail.com*

Received: 19 November 2025 Revised: 23 December 2025 Accepted: 20 January 2026 Published: 17 February 2026

Abstract *- This paper presents an intelligent ANN-Controlled Grid-Tied Solar Pv System that Supports Residential Loads, EV Charging, and Induction Motor-Based Water Pumping (Household or Agriculture) has been developed in this paper. The aim is achieved through the use of a three-phase totem pole converter with PFC to ensure a nearly unity power factor and reduce electrical loss as well as the overall strain on the grid. A boost converter is used to increase the output voltage of the solar PV array to match the DC link voltage while maximizing energy extraction from it using the Perturb and Observe (P&O) MPPT algorithm. In addition, a bidirectional buck-boost converter is used to regulate the flow of energy into/out of the battery for EV charging/discharging. An Induction Motor Drive (IMD) with SVPWM is used to operate the induction motor at maximum efficiency while also providing AC residential loads. Finally, a robust ANN controller provides real-time regulation of the DC bus voltage, controls the flow of energy between solar, EV, and the grid, and optimizes the operation of the IMD, resulting in superior dynamic response, stability, and power quality compared to conventional control methodologies. Simulation results in MATLAB demonstrate that the proposed design has better reliability, lower system losses, higher system stability, and better performance than conventional control approaches.*

Keywords *- Artificial Neural Network, Grid-connected Solar PV system, Totem-Pole Converter, Power Factor Correction, Perturb and Observe MPPT, Bidirectional Buck-Boost Converter, Electric Vehicle Charging, Induction Motor Drive.*

1. Introduction

Energy consumption continues to rise consistently in residential and commercial applications. The rising need for energy is worrying since Fossil Resources are running out. To meet the demand, the focus needs to shift to using Renewable Energy Resources (RERs) and connecting them to the utility grid [1]. The world's use of fossil fuels is being reduced because of governmental programs and subsidies to promote Renewable Energy Resources (RERs). Most governmental programs and subsidies for RERs decrease the price of the product, reduce the environmental impact, and reduce the carbon footprint, while giving governmental agencies control over "Green Power" [2]. With a reduction in the amount of traditional energy products used, there is an increase in the demand for Renewable Energy Resources. One type of renewable resource, Solar Photovoltaic (PV), has become one of the most used renewable energy resources as a result of the abundance of sunshine available in many locations, its environmentally friendly nature, and its cost competitiveness. The PV systems do not generate greenhouse gas emissions, air pollutants, or hazardous byproducts, which makes them economically attractive [3]. The PV systems require very little operational and maintenance activity to be performed, which provides reliability over almost thirty years. They can be scaled down to fit on small rooftops or up to larger commercial buildings and utility project sizes to support the decentralization of electric power generation. The PV systems also help reduce reliance on importing fossil fuels and increase grid stability and resiliency [4]. Solar energy is well-suited for a variety of domestic applications, including the charging of electric vehicles, the operation of induction motors in water pumping systems, the supply of power for household lighting and appliances, and the support of other essential residential loads. To reduce reliance on the utility grid and optimize power for EV battery charging, a solar PV system employs a Perturb and Observe (P&O) MPPT algorithm and an Artificial Neural Network (ANN) controller for maximum power extraction [5]. The PV source connects to the DC bus to meet EV battery needs. Additionally, during non-charging times or peak grid demand, the PV source and/or EV battery can supply power back to the grid, enhancing the microgrid's efficiency and reducing grid dependence [6]. AI-based MPPT offers superior tracking, rapid convergence, and reduced transients [7]. A PID controller with variable step size and GA is discussed in [8], though it is computationally intensive. Fuzzy logic MPPT controllers are explored in [9], with user expertise in membership function selection being crucial. There is a demand for reliable AI-based dc-link controllers to improve Conventional Methods. This study proposes an ANN-based MPPT to enhance PV system efficiency. The input voltage of the bidirectional DC–DC converter is interfaced with the DC bus, enabling flexible power management between the source and the EV battery. Operating in buck mode, the converter efficiently manages battery charging, while in boost mode, it supports battery discharging back to the DC bus. To achieve optimized performance, an Artificial Neural Network (ANN)-based fast-charging control strategy is employed, which regulates the duty cycle of the bidirectional DC–DC converter for accurate and efficient battery charging [10]. Solar PV systems are widely used for irrigation and water pumping in India, where 70% of agricultural land depends on irrigation due to unreliable monsoons [11].

Solar-powered Induction Motor Drives (IMDs) are favored for their reliability, cost-effectiveness, and performance in harsh conditions. Research aims to enhance the efficiency of these systems, employing techniques like Space Vector Pulse Width Modulation (SVPWM) for inverter control and integrating Artificial Neural Network (ANN) controllers for better speed regulation [12-14]. Rising residential loads for lighting, heating, and cooling have increased power demand and electricity costs. To tackle peak load demand and emissions, a model for optimal solar PV operation was proposed in [15]. Solar PV systems are increasingly popular due to their modularity and quick installation, making them ideal for residential use, reducing energy costs, and reliance on the grid [16, 17]. Grid-isolated systems like EV chargers and water pumps powered by PV arrays struggle with solar energy's intermittency, leading to unreliable power and operational shutdowns [18, 19]. Recent research favors grid-connected PV systems, enabling continuous operation by using a power allocation mechanism to draw from either the PV array or the utility grid when needed. This setup connects an ANN-based controller for EV charging and water pumping to a shared DC bus with the grid inverter, improving reliability and reducing costs [20]. Thus, grid-connected PV systems are seen as more reliable and sustainable compared to standalone systems with battery storage [21]. Maintaining grid power quality, especially Power Factor Correction (PFC), is vital for medium- and high-voltage applications and bidirectional operations like Grid-to-EV and EV-to-Grid and Solar Power Export. This work employs a three-phase bidirectional totem-pole converter that performs PFC, reduces grid power stress, and balances DC bus voltage. An Artificial Neural Network (ANN) controller enhances transient and dynamic response, ensuring stable operation for critical loads, including EV chargers, water pumping systems, and residential applications [22]. The proposed Multi-Application ANN-Controlled Solar PV Grid System using a Totem Pole Converter for EV Charging, Induction Motor Pumping, and Residential Loads is shown in Figure 1. The proposed system includes a grid-side converter acting as a bidirectional AC-DC converter for power factor correction and DC link voltage regulation. An ANN is used to manage several different tasks, including DC link voltage balancing, grid stability, solar Maximum Power Point Tracking (MPPT) control, induction motor speed regulation, and EV battery charge/discharge control. A DC-DC boost converter is utilized between the solar PV array and the DC link, where P&O MPPT is implemented along with an ANN to optimize power extraction. An efficient ANN-based EV charging system is composed of a bidirectional DC-DC buck-boost converter as well as an efficient water-pumping system using an induction motor with a three-phase SVPWM inverter on the DC link. Both systems are designed to provide high efficiency and reliability while improving both the power quality and stability of each application. In addition, the use of an ANN-based control system allows for flexibility and the ability to operate efficiently under various operating conditions.

A detailed literature review was completed to identify many combinations of Solar Photovoltaic (PV) Systems, Electric Vehicle (EV) Systems, and Utility Grids that can be controlled using various control techniques. DC link voltage regulation using a nonlinear PI controller for an Electric Vehicle (EV) charger is investigated in reference [23]. The results demonstrated an enhancement of voltage stability and better dynamic performance than with traditional controllers. An advanced hybrid converter structure for PV-EV-grid systems that can operate in five different modes to allow optimal power transfer across various operational states has been described in reference [24]. A Centralized Energy Management System for Photovoltaic (PV), Grid, Battery, and DC Load is proposed in [25]. Adaptive control for Grid-Tie PV Power Conversion Systems, including Power Factor Correction, DC-link Voltage Control, Harmonic Reduction, and Maximum Power Point Tracking (MPPT) control, as well as a power management system to generate a reference current, are described in Reference [26]. A time-based power management strategy for PV-Battery-Grid Systems is developed in [27], while [28] describes an optimal power flow method to minimize overall operating costs. Reference [29] proposed a Three-Port Integrated Topology (TPIT) that allows for integration of EVs and PV modules to provide better quality power and fewer conversions. Reference [30] presented an HPV-EVB energy management system that manages the flow of power from PV sources, EV battery banks, Home load demands, and the grid. In reference [31], an Adaptive Neuro-Fuzzy Inference System (ANFIS)-based control strategy is proposed for a grid-connected PV-powered EV charger that can improve the grid power quality during EV charging. The EV Charging Station, which uses solar and battery storage to charge vehicles, is presented in reference [32]. The authors stated that this station has high efficiency when operating in both Grid-Connected Mode and Standalone Mode. Reference [33] Presents A Control Strategy (MMGDI-AC) for Managing Grid-Connected EV charging with the use of Solar PV, and as such, focuses on the reduction of damping and safe charging of EVs. In reference [34], a solar PV-powered workplace EV charging system is designed and optimized in terms of size to minimize its dependency on the grid. In reference [35], a Proportional Regulator (PR) controller is designed and tested for a grid-tied solar-powered EV charger, providing high performance in terms of both stability and accuracy under changing conditions.

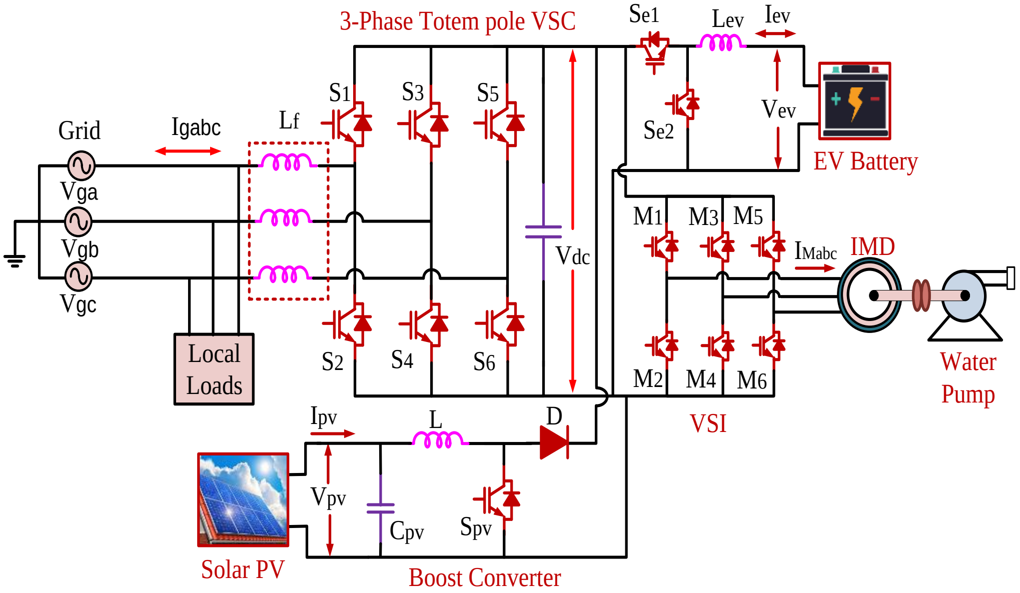

Fig. 1 Proposed system configuration

Considering the insights from the literature and the challenges discussed above, the main contributions of this work can be summarized as follows:

- The multi-application solar PV grid system is a system that can be used in many ways (e.g., EV charging, induction motor-driven water pumping, and residential Loads) as part of an integrated system architecture. The three-phase bidirectional totem pole converter allows for Power Factor Correction (PFC), DC-Link voltage balancing, and bidirectional power flow to/from the grid to provide reliable operation and high efficiency operation of the system.
- The ANN-based intelligent controller allows the controller to perform several tasks, such as MPPT of the PV array, regulate the speed of the induction motor using SVPWM, control the bidirectional Charging/Discharging of the EV Battery, and balance the grid voltage.
- This system has improved power quality due to reduced harmonic distortion and reduction of transient and dynamic disturbances, and the stress of the grid is also reduced; this results in the improvement of the overall stability, efficiency, and operation of all loads connected to the system, which are operating under variable solar irradiance and load conditions.
- The proposed system reduces the overall cost and maintenance of the system and provides a continuous and sustainable power supply for the EV Charging, Agricultural Pumping, and Household Applications; the proposed system minimizes the dependency on large battery storage systems and allows the integration of multiple functionalities within the same system.

2. Modelling and Designing of Solar PV Configuration

2.1. Formulation of Solar PV Cell

The single diode model is the most commonly employed model to represent the I-V curve behavior of a Photovoltaic (PV) cell; it captures the main Current-Voltage (I-V) characteristics of a PV cell, taking into account the effects of temperature and irradiance, and provides all the information required to compute the main performance parameters of a PV system, i.e., the Short-Circuit Current (I_{sc}), the Open-Circuit Voltage (V_{oc}), the Maximum Power (P_{max}), and the Fill Factor FF. A module is composed of several PV cells connected in Series (N_s) and in Parallel (N_p). Several modules are then connected together to form an array. Finally, the electrical energy produced by each PV array is collected and managed using a DC-DC Boost Converter, whose primary function is to regulate the terminal voltage of the PV array and enable the Maximum Power Point Tracking (MPPT) through the adjustment of its duty cycle. The MPPT ensures the highest possible conversion efficiency of the solar radiation into electrical energy, and the regulated DC voltage is fed to a DC-AC inverter to connect the PV array to the utility grid. As described above, a PV array formed by ($N_s$series-connected PV modules and (N_p) A parallel-connected module has an equivalent output current, which can be written using the Single-Diode Model as follows [36]:

$$I_{pv} = N_s I_s - N_p I_o\left(\exp\left(\frac{q\left(V_{pv}+R_s I_{pv}\right)}{AkTN_s}\right)-1\right) - N_p\frac{V_{pv}+R_s I_{pv}}{N_s R_{sh}} \qquad (1)$$

where I_s is the light-generated current, Io is the diode reverse saturation current, R_s and R_{sh} are the series and shunt resistances, q is the electron charge, k is the Boltzmann constant, T is the cell temperature, and A is the diode ideality factor.

2.2. Solar PV Boost Converter with P&O MPPT

The PV array of a Solar Photovoltaic (PV) system has nonlinear I-V characteristics that require MPPT to extract the best possible amount of energy from the PV system. The MPPT controller used in this research uses a DC-DC Boost Converter controlled by a Perturb & Observe (P&O) algorithm to control the Duty Cycle of the converter and maintain the Output Voltage at a constant level, as shown in Figure 8. While P&O is easy to implement, its efficiency under rapidly changing irradiation conditions, and also, as per the grid stability, is poor. To improve upon these issues, Artificial Neural Network (ANN)-based MPPT controllers have been introduced into the MPPT Controller, which will provide smoother operation, fewer output variations, and thus enable stable and efficient grid connection and reliable operation of EV Battery Charging Systems, as shown in Figure 4.

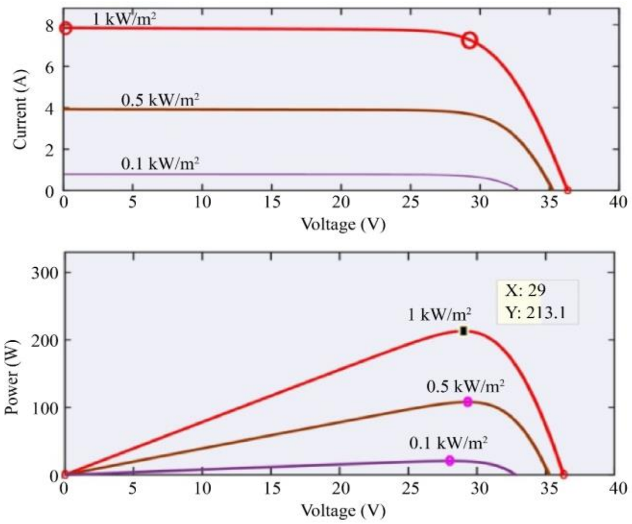

Fig. 2 V–I and P–V characteristics of a single-diode PV solar cell

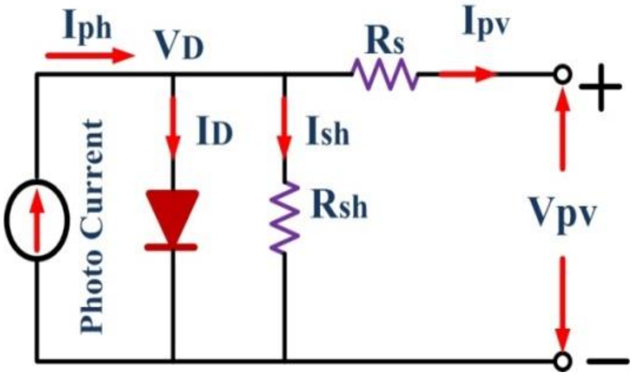

Fig. 3 Equivalent circuit model of solar PV

The steady-state equations of the boost converter are:

- Boost converter output voltage:

$$V_o = \frac{V_{pv}}{1-D} \tag{2}$$

- Boost converter input current:

$$I_{pv} = \frac{I_o}{1-D} \tag{3}$$

Where: V_{pv} and I_{pv} are the PV voltage and current, V_o is the DC link voltage, Io is the output current, and D is the duty cycle. The MPPT algorithm continuously updates D to regulate V_{pv} around the MPP.

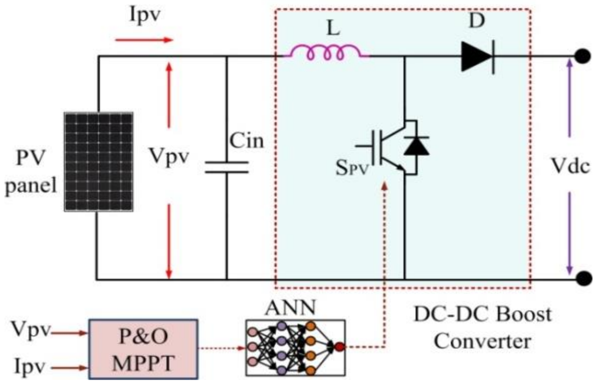

Fig. 4 Solar PV P&O MPPT DC-DC Boost Converter

Table 1. Grid Parameters

Parameters	Values
Grid Voltage (Vg)	230 V
Grid frequency (f)	50 Hz
Interface Inductor (Lf) Load Power (PL)	800μH 20 Kw

Table 2. EV Battery Parameters

Parameters	Values
Nominal Voltage	300 V
Rated Capacity	360Ah
Interface Inductor (Lf) DC Link Voltage (Vdc) DC Link Capacitor EV power (Pev)	800μH 700 V 3500 μF 10.8Kw

Table 3. Solar PV Parameters

Parameters	Values
Open circuit Voltage (Voc)	36.3 V
Short circuit current (Isc)	7.84 A
Maximum power	213.15 W
Switching frequency (fs)	5kHz
Solar boost inductor (L) Solar Power (Ppv)	2.5 mH 20 w

3. Modelling and Designing of Lithium-Ion EV Battery

3.1. Electrochemical Fundamentals

The Lithium-ion (Li-ion) batteries operate on the principle of reversible intercalation and de-intercalation of lithium ions between the graphite anode and a metal oxide cathode. The overall reaction of a Li-ion cell during charge and discharge is expressed as [37, 38]:

$$Li_xC + Li_{1-x}M_yO_z \Leftrightarrow C + L_iM_yO_z \tag{4}$$

Where:

- Li_xC represents the lithiated graphite anode,
- $Li_{1-x}M_yO_z$ represents the partially lithiated cathode (metal oxide such as $L_iC_0O_2, L_iF_ePO_4, LiMn_2O_4$),
- M is the transition metal,
- x denotes the degree of intercalation.
- At the anode (during discharge):

$$Li_xC \longrightarrow C + xLi^+ + xe^- \tag{5}$$

- At the anode (during discharge):

$$Li_{1-x}M_yO_z + xLi^+ \longrightarrow L_iM_yO_z \tag{6}$$

This reaction is reversible, enabling repeated charging and discharging cycles.

3.2. Electrical Modeling

Lithium-ion batteries are commonly represented using an Equivalent Circuit Model (ECM), which simplifies the underlying electrochemical processes while accurately capturing the electrical behavior. In this model, the terminal voltage of the cell is expressed as:

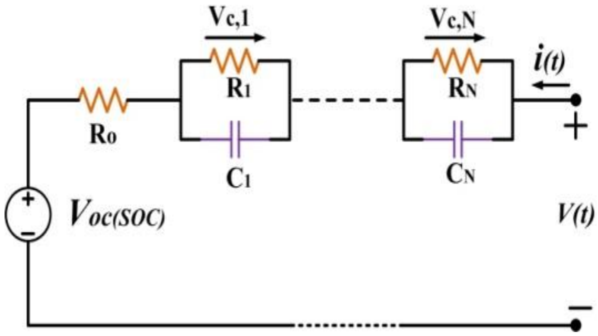

Fig. 5 Equivalent circuit diagram of lithium-ion EV battery

$$V(t) = V_{oc}(Soc) - I(t)R_s - V_{Rc}(t) \tag{7}$$

Battery Terminal Voltage $V(t)$ depends upon both the open circuit voltage, $V_{oc}(Soc)$ the Internal Resistance of the Battery, Rs, and the Polarization Voltage of the Battery, $V_{Rc}(t)$. This provides an excellent balance between complexity and accuracy in modeling battery behavior; it is suitable for use with grid integration, renewable energy storage applications, and electric vehicle charging. The state of charge, SOC, measures the available charge in relation to the nominal capacity of the battery and varies with respect to time as a function of the Coulomb counting principle.

$$SOC(t) = SOC(0) - \frac{1}{Q_{nom}} \int_0^t I(\tau)\, d\tau \tag{8}$$

Where $SOC(0)$ = Initial SOC; Q_{nom} = Nominal Battery Capacity in Ampere-Hours (Ah); and $I(\tau)$ = Instantaneous Current (positive during discharging and negative during charging); The accurate modeling of both ECM and SOC dynamics will provide a reliable means to predict system performance, manage energy efficiently, and extend the lifetime of lithium-ion batteries used in today's power systems.

3.3. ANN-Controlled EV Charging System

An Electric Vehicle (EV) charging system is an Artificial Neural Network (ANN)-controlled system that uses a bidirectional DC/DC converter to optimize both Battery charging and discharging. In Grid-To-Vehicle (G2V) mode, the bidirectional DC/DC converter is used to reduce the voltage so that the battery can be charged from the grid. In Vehicle-To-Grid (V2G) mode, it is used to boost voltage to supply energy back into the grid. Compared to the traditional PI controllers, the ANN controller has the advantage of adapting itself to dynamic conditions, which leads to improved performance with minimized overshoot and ripples, as shown in Figures 7 and 8. Additionally, the ANN controller optimizes power flow, ensures stable grid integration, and maintains reliable battery operation by monitoring important parameters.

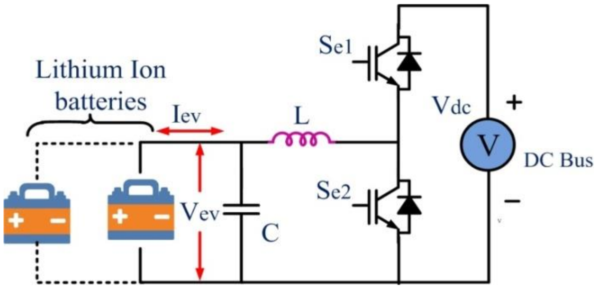

Fig. 6 Bidirectional DC-DC Converter for EV

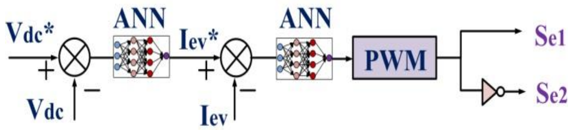

Fig. 7 EV Charging Controller

4. ANN Controller for Induction Motor Drive in Water Pumping System

The V/f-based speed controller of the induction motor structure, shown in Figure 9, regulates the Induction Motor (IM) drive speed with the aid of an Artificial Neural Network (ANN). The ANN receives the error between the reference and actual speed and generates an optimized control frequency. This frequency command, while maintaining the constant V/f ratio, is converted into sinusoidal reference signals, which are then applied to the Space Vector Pulse Width Modulation (SVPWM) block to produce the gating signals for the inverter driving the motor. Each stage of the controller is described below.

4.1. Speed Reference and Error Calculation

The reference speed for the motor is set to 1500 rpm (synchronous speed for a 2-pole machine at 50 Hz). The actual rotor speed ω_r is measured and converted from rad/s to rpm:

$$rpm = \frac{30}{\pi} \cdot \omega_r \tag{9}$$

The speed error is then obtained as:

$$e(t) = {\omega_r}^* - \omega_r \tag{10}$$

Moreover, the change in error is given by:

$$\Delta e(t) = e(t) - e(t-1) \tag{11}$$

Both e(t) and $\Delta e(t)$ form the ANN inputs

Table 4. IMD parameters

Parameters	Values
IMD Voltage (Vim)	700 V
IMD frequency (f)	50 Hz
Stator resistance (R_s)	0.9968 Ω
Rotor resistance (R_r)	0.6258 Ω
Stator inductance (L_s)	0.0001495 H
Rotor inductance (L_s)	0.005473 H
Mutual Inductance (L_m)	0.0354 H
Inertia (J)	0.05 kg. m^2
Friction factor	0.005879 (N.m.s)
IMD Poles (P)	4
IMD Power	6 Kw

4.2. ANN Controller

The reference speed for the motor is set to 1500 rpm (synchronous speed for a 4-pole machine at 50 Hz). The actual rotor speed ω_r is measured and converted from rad/s to rpm:

$$f = \frac{P}{120} \cdot rpm \tag{12}$$

Where P is the number of poles

The corresponding electrical angular frequency is:

$$\omega_e = 2\pi f \tag{13}$$

4.3. Frequency Limitation

To ensure safe motor operation and avoid exceeding the rated synchronous speed, the generated frequency is limited as:

$$0 \le f_e \le f_{rated} \tag{14}$$

Where f_{rated} is the rated supply frequency (50 Hz).

4.4. Sinusoidal Reference Generation

The limited angular frequency ω_e is integrated to obtain the instantaneous electrical angle:

The limited angular frequency ω_e is integrated to obtain the instantaneous electrical angle:

$$\theta(t) = \int \omega_e \, dt \tag{15}$$

Three sinusoidal phase reference signals with a 120-degree∘ phase displacement are then generated:

$$V_a^* = sin(\omega t) \tag{16}$$

$$V_b^* = \sin(\omega t - 120°) \tag{17}$$

$$V_c^* = \sin(\omega t - 240^0) \tag{18}$$

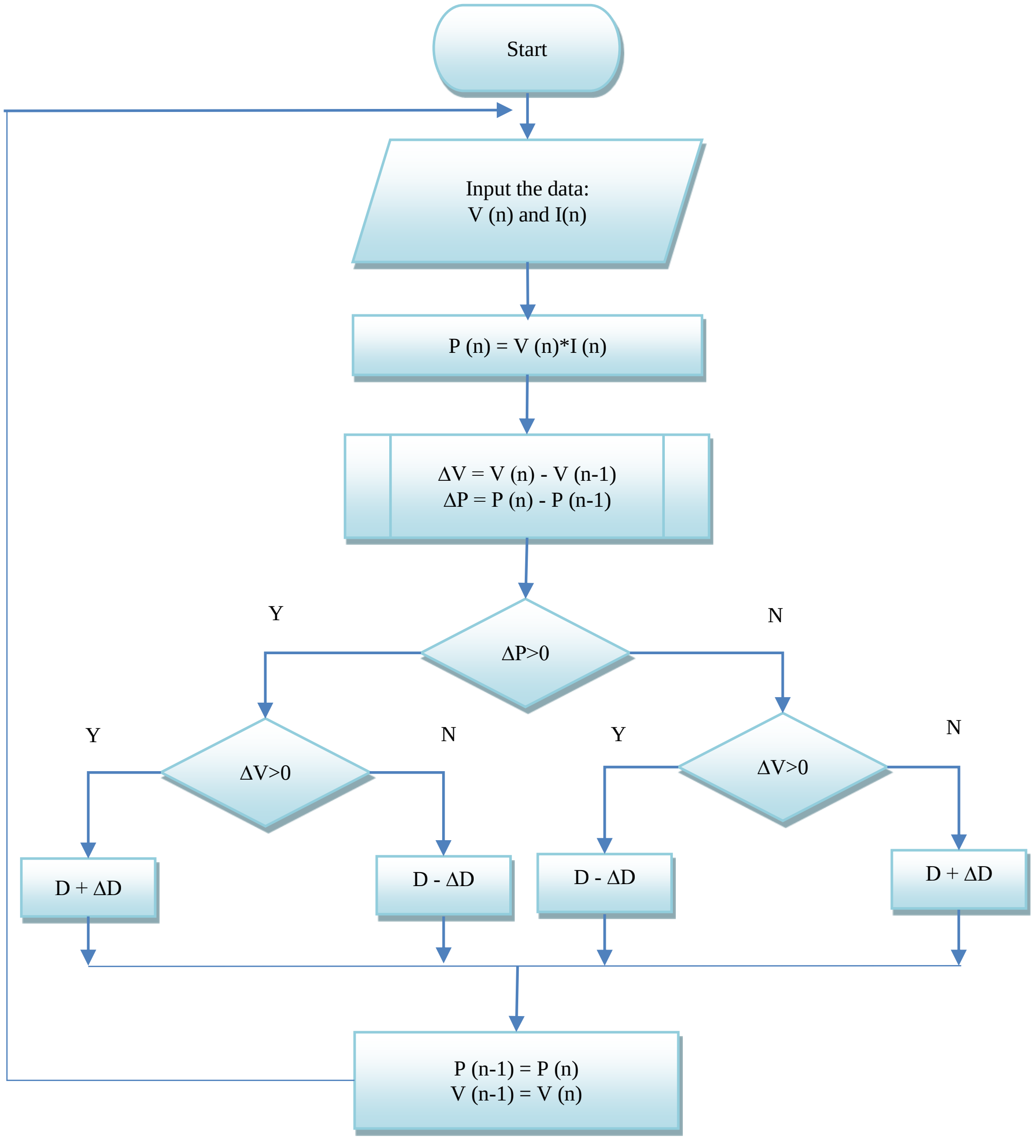

Fig. 8 Flowchart of the P&O algorithm, implemented in the controller model

4.5. Sinusoidal Reference Generation

The three reference signals are normalized by the SVPWM factor to ensure they remain within the modulation hexagon boundary:

$$\mathrm{V_{x,norm}} = \frac{2}{\sqrt{3}} \cdot \mathrm{V_x^*}(\mathrm{x = a, b, c}) \tag{19}$$

To confine the references within the PWM comparison range, an offset of +0.5 is injected:

$$\mathrm{V_{x,offset}} = \mathrm{V_{x,norm}} + 0.5 \tag{20}$$

This guarantees all modulation signals remain within [0, 1].

4.6. Maximum–Minimum Signal Processing

At every instant, the maximum and minimum among the three sinusoidal references are identified:

$$V_{max} = \max(V_a^*, V_b^*, V_c^*) \tag{21}$$

$$V_{min} = \min(V_a^*, V_b^*, V_c^*) \tag{22}$$

The zero-sequence (offset) component is computed as:

$$V_{offset} = -\frac{V_{max}+V_{min}}{2} \tag{23}$$

This offset is added to all three reference signals:

$$V_{a,shift} = V_a^* + V_{offset} \tag{24}$$

$$V_{b,shift} = V_b^* + V_{offset} \tag{25}$$

$$V_{c,shift} = V_c^* + V_{offset} \tag{26}$$

This process centers the three references symmetrically within the carrier window, maximizing DC bus utilization and reducing harmonic distortion.

Additionally:

- A positive offset (+0.5) is added to ensure signals lie in the [0, 1] modulation range.
- A negative offset (–0.5) is applied to generate complementary references for the lower inverter switches.

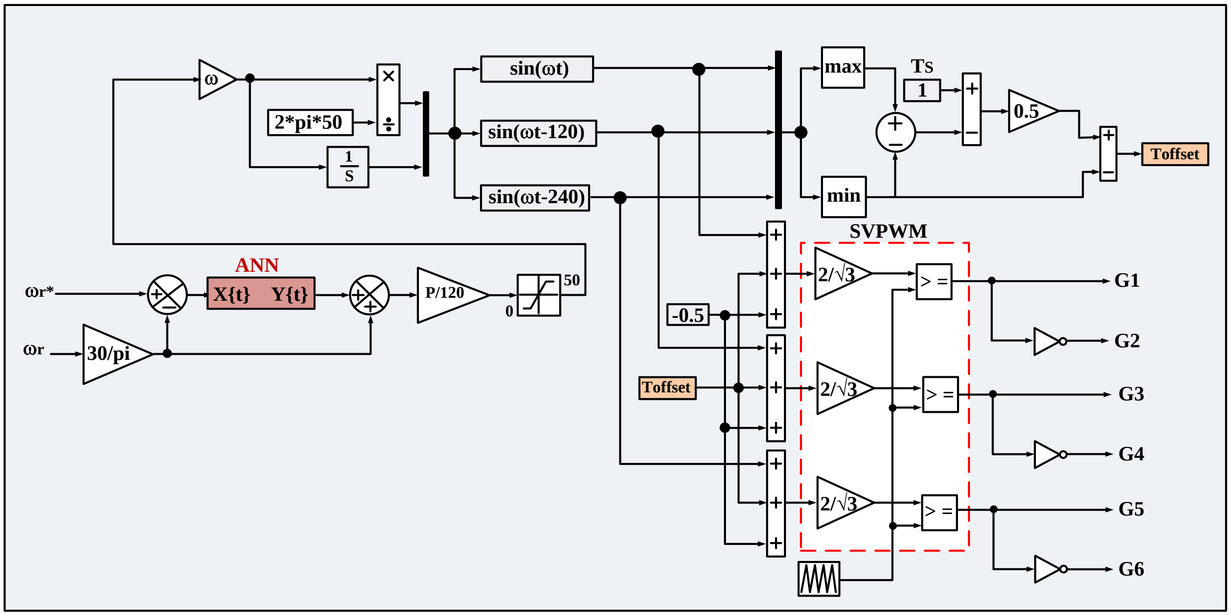

Fig. 9 V/f-based speed controller of the induction motor drive for the water pumping system

4.7. SVPWM Signal Generation

The processed sinusoidal reference signals are compared against a high-frequency triangular carrier waveform:

$$M_x = \begin{cases} 1, & if\ V_{x,shift} \geq V_{carrier} \\ 0, & otherwise \end{cases} \quad (x = a,b,c) \tag{27}$$

Thus, six gating pulses (M1-M6) are generated for the inverter switches.

4.8. Inverter and Motor Drive

The inverter outputs the three-phase voltages corresponding to the ANN-regulated reference. These are applied to the induction motor, where the electromagnetic torque is computed as:

$$T_e = \frac{3}{2} \cdot \frac{P}{2} \cdot \left(\psi_{ds} i_{qs} - \psi_{qs} i_{ds}\right) \tag{28}$$

The mechanical dynamics are expressed as:

$$J\frac{d\omega_r}{dt} + B\omega_r = T_e - T_L \quad (29)$$

The ANN controller ensures that $\omega_r \approx \omega_r*$, maintaining a constant water flow rate under varying operating conditions.

5. Totem Pole Converter Controller

The totem pole bridgeless converter is a high-efficiency AC-to-DC power converter that is widely used in electric vehicle systems, as well as in renewable energy systems. The bridgeless nature of this totem pole converter results in significantly less loss when compared to other converters and enables the ability to achieve higher power factors when using PFC (Power Factor Correction) techniques. As seen in Figure 10, a traditional PI-based control strategy has many limitations, including the need for very slow responses and poor adaptability; these limitations are to be addressed by the proposed Artificial Neural Network (ANN)-based controller. The proposed ANN controller contains two separate ANNs.

The first ANN is responsible for controlling the DC link voltage. The second ANN is used to track the desired currents accurately at the same time, ensuring synchronization with the grid voltages. As well as coordinating switching actions between the two ANNs, a zero-crossing detection method will coordinate the switching action to enable bridgeless operation. In comparison to the PI control strategy, the ANN-based control strategy provides much faster transient responses, lower Total Harmonic Distortion (THD), and near unity power factor performance, all of which make the ANN-based control strategy very attractive for high-performance applications.

5.1. DC Bus Error and ANN Voltage Controller

The reference DC Bus Voltage (V_{dc}^*) is compared with the actual measured DC Voltage (V_{dc}). The error is expressed as:

$$e_v(t) = V_{dc}^* - V_{\mathrm{dc}} \quad (30)$$

This error is applied to the first ANN controller, which outputs a reference current magnitude. I_{ref}. The ANN ensures nonlinear dynamic regulation for better transient stability compared to PI control.

5.2. Grid Voltage Normalization (Phase Templates)

The three-phase grid voltages are:

$$V_{ga}(t),\ V_{gb}(t),\ V_{gc}(t) \quad (31)$$

Their RMS magnitude is:

$$V_{g,rms} = \sqrt{\frac{1}{T}\int_0^T (V_{ga}^2 + V_{gb}^2 + V_{gc}^2)\, dt} \quad (32)$$

The unit templates for each phase are obtained as:

$$u_a(t) = \frac{V_{ga}(t)}{V_{g,rms}}, u_b(t) = \frac{V_{gb}(t)}{V_{g,rms}}, u_c(t) = \frac{V_{gc}(t)}{V_{g,rms}} \quad (33)$$

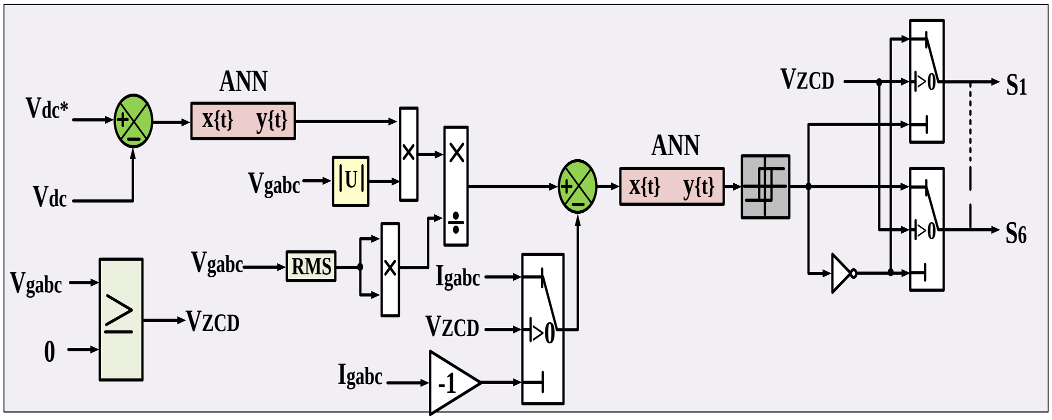

Fig. 10 Controller design of 3-phase totem pole converter

5.3. Reference Current Generation

The ANN output references the current magnitude. I_{ref} is multiplied by each unit template to produce the reference input currents for all three phases:

$$I_a^{ref}(t) = I_{ref} \cdot u_a(t) \quad (34)$$

$$I_b^{ref}(t) = I_{ref} \cdot u_b(t) \quad (35)$$

$$I_c^{ref}(t) = I_{ref} \cdot u_c(t) \quad (36)$$

Thus, the reference current of each phase remains sinusoidal and in-phase with its respective voltage.

5.4. Actual Current Measurement and Error Calculation

The actual grid currents are measured:

$$I_{ga}(t), I_{gb}(t), I_{gc}(t) \quad (37)$$

The phase-wise current errors are computed as:

$$e_{ia}(t) = I_a^{ref}(t) - I_{ga}(t) \tag{38}$$

$$e_{ib}(t) = I_b^{ref}(t) - I_{gb}(t) \tag{39}$$

$$e_{ic}(t) = I_c^{ref}(t) - I_{gc}(t) \tag{40}$$

These errors are fed into the second ANN controller for duty ratio computation.

5.5. ANN Current Controller (Duty Ratios)

The ANN generates the duty cycles for each phase:

$$D_a(t) = ANN\big(e_{ia}(t)\big), D_b(t) = ANN\big(e_{ib}(t)\big), D_c(t) = N\big(e_{ic}(t)\big) \tag{41}$$

These duty ratios regulate the switching states of the totem-pole converter.

5.6. Zero-Crossing Detection with Grid Current

In addition to voltage zero-crossing, the grid current is also checked to ensure correct phase alignment and polarity switching. The measured three-phase grid currents are:

$$I_{ga}(t),\ I_{gb}(t), I_{gc}(t) \tag{42}$$

For each phase, a sign check is performed:

$$ZCD_{ia}(t) = \begin{cases} 1, & I_{ga}(t) \geq 0 \\ 0, & I_{ga}(t) < 0 \end{cases} \tag{43}$$

$$ZCD_{ib}(t) = \begin{cases} 1, & I_{gb}(t) \geq 0 \\ 0, & I_{gb}(t) < 0 \end{cases} \tag{44}$$

$$ZCD_{ic}(t) = \begin{cases} 1, & I_{gc}(t) \geq 0 \\ 0, & I_{gc}(t) < 0 \end{cases} \tag{45}$$

This current-based ZCD works as a complementary check to the voltage-based ZCD. It ensures that switch commutation only occurs when both current and voltage polarities are consistent, preventing shoot-through and distortion.

5.7. Switching Signal Generation with Voltage & Current ZCD

For each phase, the gating signals are now generated as a function of duty ratio, voltage ZCD, and current ZCD:

Phases A, B, and C:

$$S_1 = f(D_a, ZCD_{va}, ZCD_{ia}),\ S_1 = \bar{S}_2 \tag{46}$$

$$S_3 = f(D_b, ZCD_{vb}, ZCD_{ib}),\ S_3 = \bar{S}_4 \tag{47}$$

$$S_5 = f(D_c, ZCD_{vc}, ZCD_{ic}),\ S_5 = \bar{S}_6 \tag{48}$$

Here:

- ZCD_v = Zero-crossing from grid voltage
- ZCD_i = Zero-crossing from grid current

The combined ZCD logic ensures that upper switches conduct during positive polarity (both current and voltage positive), while lower switches conduct during negative polarity, providing robust phase alignment for bridgeless PFC operation.Unity power factor with stable switching:

$$I_{ga}(t) \parallel V_{ga}(t), I_{gb}(t) \parallel V_{gb}(t), I_{gc}(t) \parallel V_{gc}(t) \tag{49}$$

6. Designing the ANN Controller

The ANN controller is designed to approximate the nonlinear control law of the system. It processes input signals (error and change of error) through multiple layers, each applying a weighted summation followed by a nonlinear activation function, as shown in Figure 11. The following steps explain the mathematical design in detail.

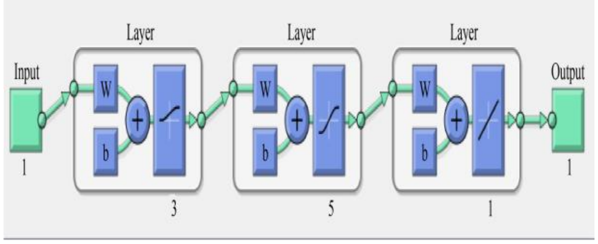

Fig. 11 Structure of Neural Network

6.1. Error Signal Computation

The controller input is based on the deviation between the reference signal and the actual system output.

$$e(t) = r(t) - y(t) \tag{50}$$

Where: r(t): reference signal (desired output, e.g., voltage or speed), y(t): actual measured system output, e(t): instantaneous error. The rate of change of error is also included as an additional input:

$$\Delta e(t) = e(t) - e(t-1) \tag{51}$$

Thus, the ANN input vector becomes:

$$x(t) = \begin{bmatrix} e(t) \\ \Delta e(t) \end{bmatrix} \tag{52}$$

This ensures that the controller has both the present error and the trend of error variation for better prediction of the control action.

6.2. General ANN Mapping

The ANN approximates a nonlinear mapping function:

$$u(t) = fANN(x(t), w, b) \tag{53}$$

Where: u(t): control output (e.g., duty cycle), x(t): input vector [e(t), Δe(t)], W,b: weights and biases of neurons, $fANN$: nonlinear transformation through activation functions.

6.3. Input to First Hidden Layer

Each neuron in the first hidden layer performs a weighted summation of the inputs:

$$z_1 = W_1 x(t) + b_1 \tag{54}$$

Where: W_1 weight matrix of the first hidden layer, b1bias vector of the first hidden layer.

The activation function applied is the log-sigmoid (logsig):

$$h_1 = f_1(z_1) = logsig(z_1) = \frac{1}{1+e^{-z_1}} \tag{55}$$

- Logsig compresses the output into the range [0,1]. It ensures smooth and bounded nonlinear mapping. Suitable for representing normalized nonlinear responses.

6.4. First Hidden Layer to Second Hidden Layer

The outputs from the first hidden layer are again combined using weights and biases:

$$z_2 = w_2 h_1 + b_2 \tag{56}$$

The activation function applied here is tangent-sigmoid (tansig):

$$h_2 = f_2(z_2) = tansig(z_2) = \frac{2}{1+e^{-2z_2}} - 1 \tag{57}$$

$tansig$ is equivalent to the hyperbolic tangent function:

$$\tanh(z) = \frac{e^z - e^{-z}}{e^z + e^{-z}} \tag{58}$$

- The range is [−1, +1].
- Symmetry around zero allows handling of both positive and negative control actions.

6.5. Output Layer

The second hidden layer outputs are linearly combined:

$$z_3 = W_3 h_2 + b_3 \tag{59}$$

The activation function at the output is purelin (linear):

$$u(t) = f_3(z_3) = purelin(z_3) = z_3 \tag{60}$$

6.6. Training Objective

The ANN parameters (W, b) are tuned by minimizing the Mean Squared Error (MSE):

$$E = \frac{1}{N}\sum_{k=1}^{N}[T(k) - u(k)]^2 \tag{61}$$

Where: T(k): target control output (from reference or existing controller), u(k): ANN predicted control output, N: total number of training samples

6.7. Weight Update Rule (Levenberg–Marquardt Algorithm)

The weights are updated iteratively:

$$W^{new} = W^{old} - (J^T J + \mu I)^{-1} J^T e \tag{62}$$

Where: J: Jacobian matrix of error function, e: error vector between ANN output and target, μ: learning parameter (controls step size)

This ensures fast convergence and stability during training.

6.8. Closed-Loop ANN Controller

The trained ANN is placed inside the control loop as:

$$r(t) \longrightarrow [e(t), \Delta e(t)] \xrightarrow{ANN} u(t) \xrightarrow{Plant} y(t) \tag{63}$$

Where: $r(t)$: reference signal, $[e(t), \Delta e(t)]$: ANN inputs, u(t): ANN control output, y(t): system response

7. Simulation Results and Discussion

The performance of the proposed ANN-based control of a 20 kW-rated solar PV grid system that can be applied to different applications (EV Charging, Induction Motor Water Pumping, and Residential Load Support) has been demonstrated by simulation using the MATLAB/Simulink environment. The model was composed of a Boost Converter with a Perturb and Observe (P&O) Maximum Power Point Tracking (MPPT) algorithm; the P&O MPPT Algorithm successfully tracked the MPP under varying operating conditions. The simulation run time was 2 seconds with solar irradiance beginning at 300 W/m² (and generating 6 kW from 0 to 0.3 sec). The irradiance then increased to 600 W/m², and the system generated 12 kW from 0.3 to 0.45 sec. At 0.45 sec, the system's peak irradiance reached 1000 W/m² and generated 20 kW until the end of the simulation at 2 seconds.

As solar energy increased, the system reduced its dependence on the utility grid to meet load demands. Additionally, the ANN controller reduced transients and improved the dynamic response of the system, improving overall grid power quality through the reduction of nonlinearities in both solar voltage and current, as seen in the simulation results in Figure 12. A three-phase totem-pole converter was evaluated under varying loads and achieved a high power factor of 0.998 and reduced Total Harmonic Distortion (THD) of grid current from 3.40 % (PI controller) to 2.44 %, meeting IEEE-519 standards as shown in Figure 13. The ANN controller improved the smoothness of the switching transitions and the efficiency of the system while also maintaining a stable DC-link voltage during dynamic changes. The bidirectional buck-boost converter was also capable of regulating both the charging and discharging cycles for EV charging; it maintained a consistent charging current profile throughout each cycle. Charging began at 1.5 sec with 25 A and increased to 50 A by 1.7 sec and decreased to 35 A until stabilization. The Induction Motor Drive (IMD) for water pumping also showed outstanding performance and smooth torque response utilizing SVPWM.

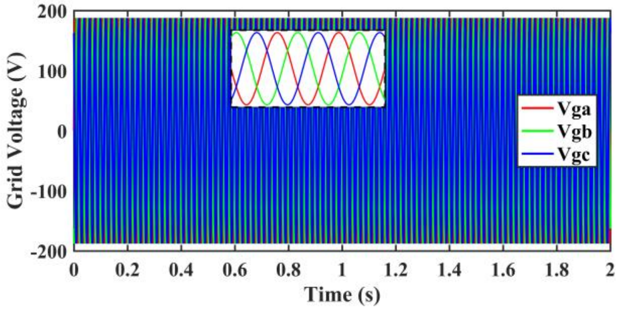

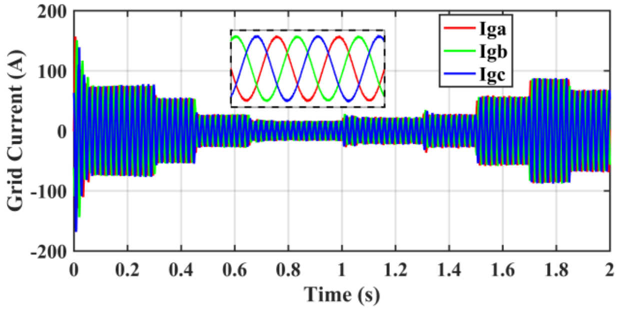

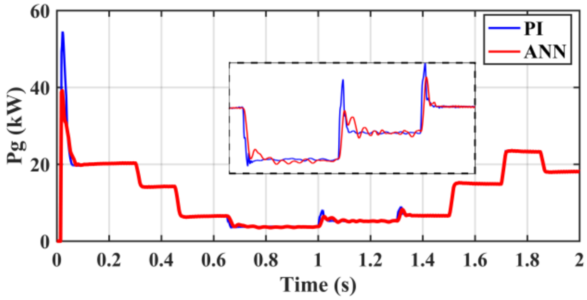

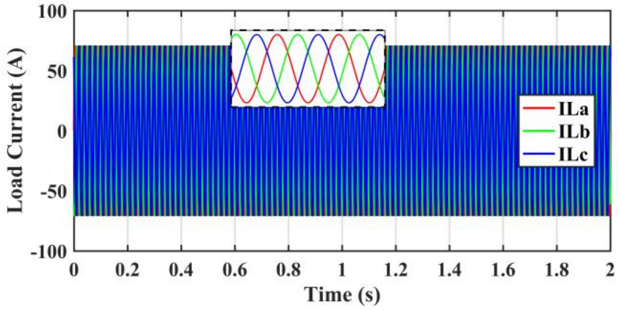

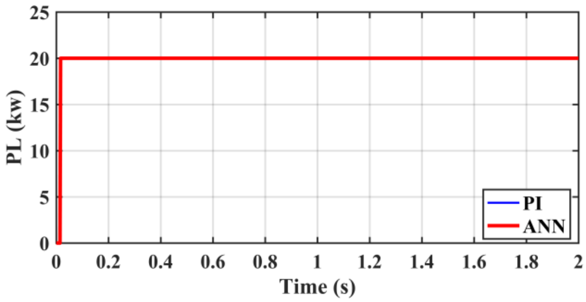

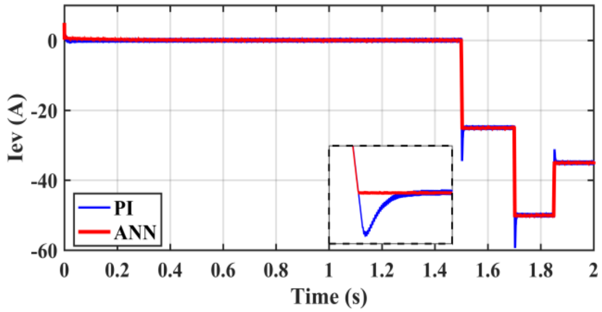

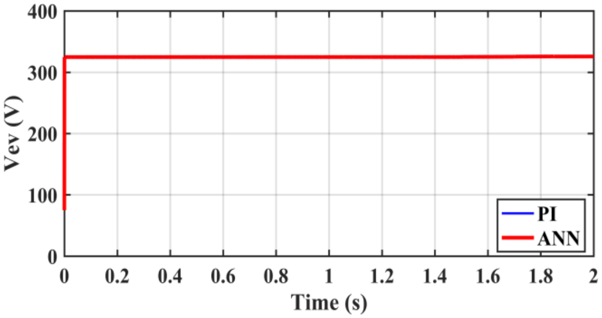

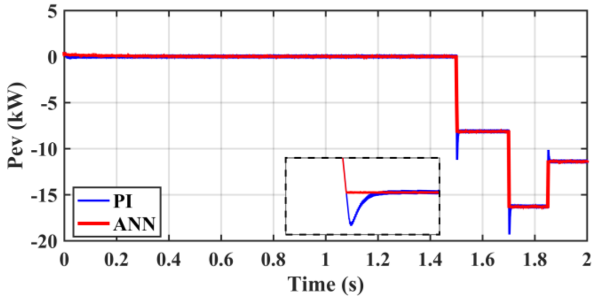

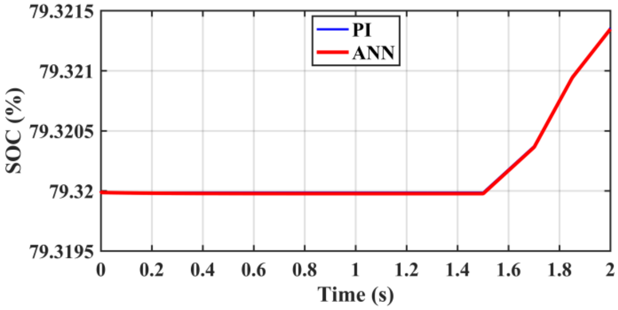

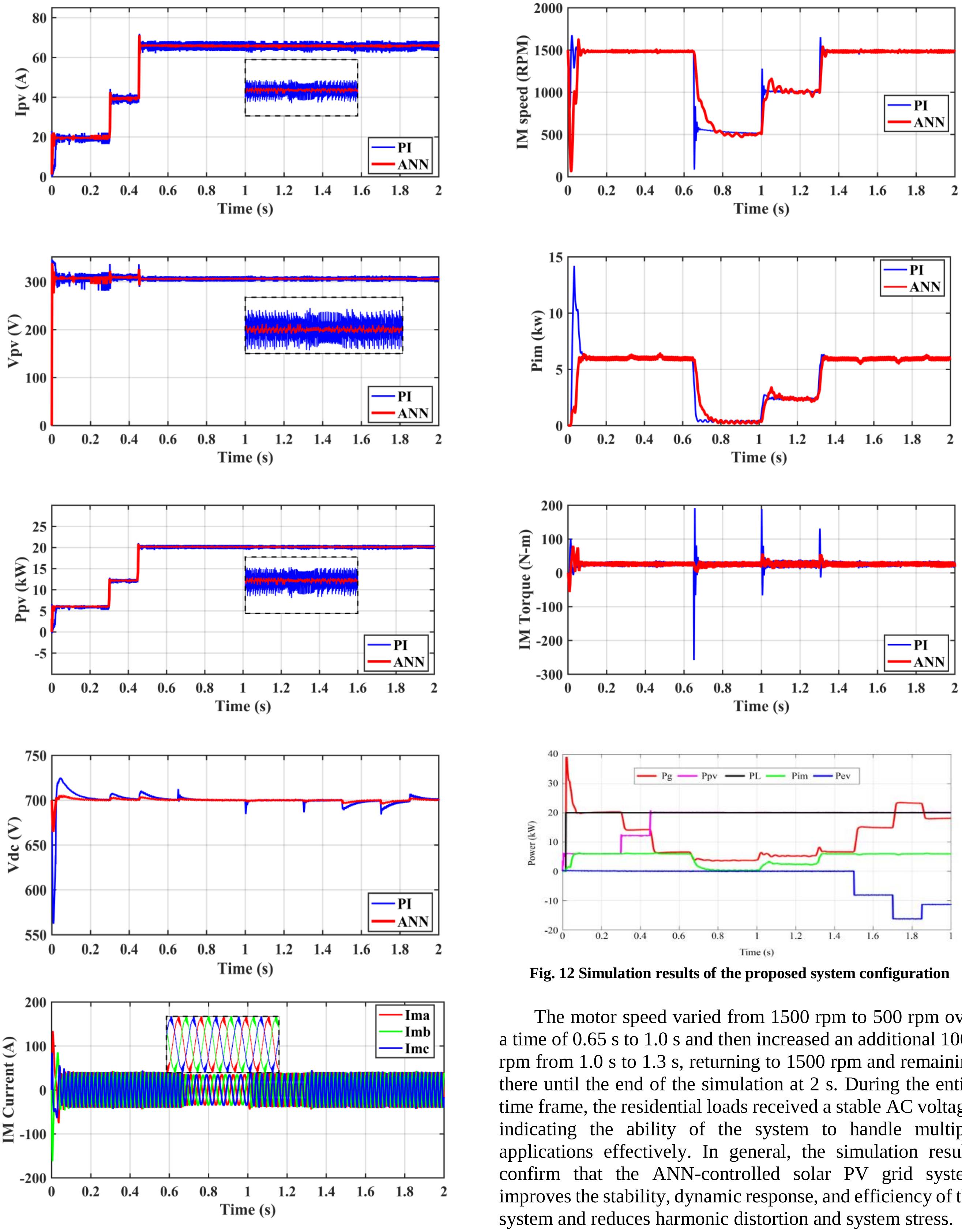

Fig. 12 Simulation results of the proposed system configuration

The motor speed varied from 1500 rpm to 500 rpm over a time of 0.65 s to 1.0 s and then increased an additional 1000 rpm from 1.0 s to 1.3 s, returning to 1500 rpm and remaining there until the end of the simulation at 2 s. During the entire time frame, the residential loads received a stable AC voltage, indicating the ability of the system to handle multiple applications effectively. In general, the simulation results confirm that the ANN-controlled solar PV grid system improves the stability, dynamic response, and efficiency of the system and reduces harmonic distortion and system stress.

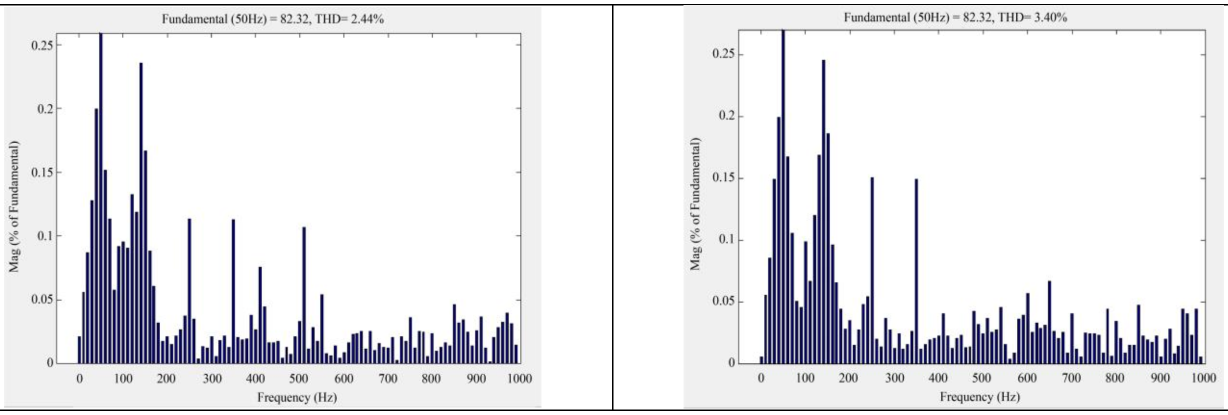

Fig. 13 Grid current THD: (a) with ANN, and (b) with PI controller.

Table 5. Comparative analysis of system configurations with respect to controller operation

Connected sources/Loads	Control strategies	Current control feature	References
Solar PV, Grid, EV	DC-Link Voltage, MPPT, EV battery charging/discharging	Power quality improvement	[23]
Grid, Solar PV, EV, BES	DC link voltage, EV battery charging/discharging, BES harging/discharging,	Power quality improvement	[24]
Grid, solar PV, EV, BES	DC link voltage, EV battery charging/discharging, BES charging/discharging, Reactive power	Power quality improvement	[25]
Grid, EV, solar PV, BES	DC link voltage, EV battery, charging/discharging, BES charging/discharging, Reactive power	Power quality improvement	[26]
Grid, solar PV, EV	DC link voltage, PFC, EV battery charging/discharging	Power factor correction	[27]
Grid, solar PV, EV	DC link voltage, PFC, Mode switching	Power factor correction	[28]
Grid, PV, EV battery	DC link voltage, PFC, MPPT, EV battery charging/discharging	Power factor correction	[29]
Grid, solar PV, EV, IMD, Residential Loads	DC link voltage, PFC, MPPT, EV battery charging/discharging	Power factor correction with system stability	Proposed ANN controller

8. Conclusion

This paper describes an Artificial Neural Network (ANN)-Controlled Solar Photovoltaic (PV) grid-connected system that was designed to provide integrated EV charging, induction motor water pumping, and residential load supply. The system includes a solar PV array, a P&O MPPT boost converter, a three-phase totem-pole converter to improve the power factor correction, a bidirectional Buck-Boost Converter to charge/discharge an electric vehicle, and an Induction Motor Drive (IMD) using Space Vector Pulse Width Modulation (SVPWM). The simulation results demonstrate that the ANN controller improved the system's performance by rapidly tracking the Maximum Power Point (MPP), stabilizing the DC bus voltage, and reducing voltage and current ripples. When compared to PI Control, the ANN controller provided improved dynamic response, reduced grid current Total Harmonic Distortion (THD) to less than 3%, and maintained near unity power factor, therefore improving grid power quality. The system was able to provide robust regulation of the SOC of the EV battery, smooth torque and speed of the induction motor, and reliable residential load supplies under varied environmental and operational conditions. This ANN-based approach provided stability, power quality, and efficiency while reducing dependencies on the grid.

References

[1] Godfrey Boyle, *Renewable Electricity and the Grid: The Challenge of Variability*, 1st ed., Routledge, 2007. [Google Scholar] [Publisher Link]

[2] Ahmed Yousuf Saber, and Ganesh Kumar Venayagamoorthy, "Plug-in Vehicles and Renewable Energy Sources for Cost and Emission Reductions," *IEEE Transactions on Industrial Electronics*, vol. 58, no. 4, pp. 1229-1238, 2011. [CrossRef] [Google Scholar] [Publisher Link]

[3] Takhir M. Razykov et al., “Solar Photovoltaic Electricity: Current Status and Future Prospects,” *Solar Energy*, vol. 85, no. 8, pp. 1580-1608, 2011. [CrossRef] [Google Scholar] [Publisher Link]

[4] Nadarajah Kannan, and Divagar Vakeesan, “Solar Energy for Future World: - A Review,” *Renewable and Sustainable Energy Reviews*, vol. 62, pp. 1092-1105, 2016. [CrossRef] [Google Scholar] [Publisher Link]

[5] Shaik Rafi Kiran et al., “Reduced Simulative Performance Analysis of Variable Step Size ANN based MPPT Techniques for Partially Shaded Solar PV Systems,” *IEEE Access*, vol. 10, pp. 48875-48889, 2022. [CrossRef] [Google Scholar] [Publisher Link]

[6] Samir M. Shariff et al., “System Design and Realization of a Solar-Powered Electric Vehicle Charging Station,” *IEEE Systems Journal*, vol. 14, no. 2, pp. 2748-2758, 2020. [CrossRef] [Google Scholar] [Publisher Link]

[7] Sara Allahabadi, Hossein Iman-Eini, and Shahrokh Farhangi, “Fast Artificial Neural Network based Method for Estimation of the Global Maximum Power Point in Photovoltaic Systems,” *IEEE Transactions on Industrial Electronics*, vol. 69, no. 6, pp. 5879-5888, 2022. [CrossRef] [Google Scholar] [Publisher Link]

[8] Adeel Feroz Mirza et al., “Advanced Variable Step Size Incremental Conductance MPPT for a Standalone PV System Utilizing a GA-Tuned PID Controller,” *Energies*, vol. 13, no. 16, pp. 1-24, 2020. [CrossRef] [Google Scholar] [Publisher Link]

[9] Carlos Robles Algarín, John Taborda Giraldo, and Omar Rodríguez Álvarez, “Fuzzy Logic based MPPT Controller for a PV System,” *Energies*, vol. 10, no. 12, pp. 3-18, 2017. [CrossRef] [Google Scholar] [Publisher Link]

[10] Bikash Sah, Praveen Kumar, and Sanjay Kumar Bose, “A Fuzzy Logic and Artificial Neural Network-based Intelligent Controller for a Vehicle-to-Grid System,” *IEEE Systems Journal*, vol. 15, no. 3, pp. 3301-3311, 2021. [CrossRef] [Google Scholar] [Publisher Link]

[11] Jyoti Maurya, and R.K. Saket, “Performance Analysis of Single-Stage and Two-Stage VSI-Fed IM Drive for Solar Pump Irrigation Systems,” *2023 IEEE IAS Global Conference on Renewable Energy and Hydrogen Technologies (GlobConHT)*, Male, Maldives, pp. 1-6, 2023. [CrossRef] [Google Scholar] [Publisher Link]

[12] Sachin Jain, Ramsha Karampuri, and V.T. Somasekhar, “An Integrated Control Algorithm for a Single-Stage PV Pumping System using an Open-End Winding Induction Motor,” *IEEE Transactions on Industrial Electronics*, vol. 63, no. 2, pp. 956-965, 2016. [CrossRef] [Google Scholar] [Publisher Link]

[13] Subrata K. Mondal, Joao O.P. Pinto, and Bimal K. Bose, “A Neural-Network-based Space-Vector PWM Controller for a Three-Level Voltage-Fed Inverter Induction Motor Drive,” *IEEE Transactions on Industry Applications*, vol. 38, no. 3, pp. 660-669, 2002. [CrossRef] [Google Scholar] [Publisher Link]

[14] Suman Maiti et al., “An Adaptive Speed Sensorless Induction Motor Drive with Artificial Neural Network for Stability Enhancement,” *IEEE Transactions on Industrial Informatics*, vol. 8, no. 4, pp. 757-766, 2012. [CrossRef] [Google Scholar] [Publisher Link]

[15] Simon Le Blond et al., “Cost and Emission Savings from the Deployment of Variable Electricity Tariffs and Advanced Domestic Energy Hub Storage Management,” *2014 IEEE PES General Meeting | Conference and Exposition, National Harbor*, MD, USA, pp. 1-5, 2014. [CrossRef] [Google Scholar] [Publisher Link]

[16] Ahad Kazemi, and M. Sadeghi, “Sitting and Sizing of Distributed Generation for Loss Reduction,” *2009 Asia-Pacific Power and Energy Engineering Conference*, Wuhan, China, pp. 1-4, 2009. [CrossRef] [Google Scholar] [Publisher Link]

[17] Thanhtung Ha et al., “Energy Hub Modeling to Minimize Residential Energy Costs Considering Solar Energy and BESS,” *Journal of Modern Power Systems and Clean Energy*, vol. 5, no. 3, pp. 389-399, 2017. [CrossRef] [Google Scholar] [Publisher Link]

[18] Sara Ghaem Sigarchian, Anders Malmquist, and Torsten Fransson, “Modeling and Control Strategy of a Hybrid PV/Wind/Engine/Battery System to Provide Electricity and Drinkable Water for Remote Applications,” *Energy Procedia*, vol. 57, pp. 1401-1410, 2014. [CrossRef] [Google Scholar] [Publisher Link]

[19] Abla Khiareddine, Chokri Ben Salah, and Mohamed Faouzi Mimouni, “Strategy of Energy Control in PVP/Battery Water Pumping System,” *2014 First International Conference on Green Energy ICGE 2014*, Sfax, Tunisia, pp. 49-54, 2014. [CrossRef] [Google Scholar] [Publisher Link]

[20] Prabhat Ranjan Bana, Mohammad Amin, and Marta Molinas, “ANN-based Surrogate PI and MPC Controllers for Grid-Connected VSC System: Small-Signal Analysis and Comparative Evaluation,” *IEEE Journal of Emerging and Selected Topics in Power Electronics*, vol. 12, no. 1, pp. 566-578, 2024. [CrossRef] [Google Scholar] [Publisher Link]

[21] M. Huang, “Photovoltaic Water Pumping and Residual Electricity Grid- Connected System,” *Chinese Patent CN 204131142*, 2015. [Google Scholar]

[22] Prabhat Ranjan Bana, Salvatore D’Arco, and Mohammad Amin, “ANN-based Robust Current Controller for Single-Stage Grid-Connected PV with Embedded Improved MPPT Scheme,” *IEEE Access*, vol. 12, pp. 100251-100262, 2024. [CrossRef] [Google Scholar] [Publisher Link]

[23] Doğan Çelik, and Hafiz Ahmed, “Enhanced Control of Superconducting Magnetic Energy Storage Integrated UPQC for Power Quality Improvement in EV Charging Station,” *Journal of Energy Storage*, vol. 62, pp. 1-16, 2023. [CrossRef] [Google Scholar] [Publisher Link]

[24] K.S. Raja Sekhar, Madhuri A. Chaudhari, and Vinod Khadkikar, “Enhanced Hybrid Converter Topology for PV-Grid-EV Integration,” *IEEE Transactions on Energy Conversion*, vol. 38, no. 4, pp. 2634-2646, 2023. [CrossRef] [Google Scholar] [Publisher Link]

[25] Chandrakant L. Bhattar, and Madhuri A. Chaudhari, “Centralized Energy Management Scheme for Grid Connected DC Microgrid,” *IEEE Systems Journal*, vol. 17, no. 3, pp. 3741-3751, 2023. [CrossRef] [Google Scholar] [Publisher Link]

[26] SeokJu Kang, Jinah Noh, and Jung-Wook Park, “Active Distribution Management System based on Smart Inverter Control of PV/ESS Integrated System,” *IEEE Transactions*, vol. 69, no. 8, pp. 7994-8003, 2022. [CrossRef] [Google Scholar] [Publisher Link]

[27] Priyanka Kishor Sorte, Kaibalya Prasad Panda, and Gayadhar Panda, “Current Reference Control based MPPT and Investigation of Power Management Algorithm for Grid-Tied Solar PV-Battery System,” *IEEE Systems Journal*, vol. 16, no. 1, pp. 386-396, 2022. [CrossRef] [Google Scholar] [Publisher Link]

[28] Pablo García-Triviño et al., “Supervisory Control System for a Grid-Connected MVDC Microgrid based on Z-Source Converters with PV, Battery Storage, Green Hydrogen System and Charging Station of Electric Vehicles,” *IEEE Transactions on Industry Applications*, vol. 59, no. 2, pp. 2650-2660, 2023. [CrossRef] [Google Scholar] [Publisher Link]

[29] Vítor Monteiro, J. Gabriel Pinto, and João Luiz Afonso, “Experimental Validation of a Three-Port Integrated Topology to Interface Electric Vehicles and Renewables with the Electrical Grid,” *IEEE Transactions on Industrial Informatics*, vol. 14, no. 6, pp. 2364-2374, 2018. [CrossRef] [Google Scholar] [Publisher Link]

[30] Viet Thang Tran et al., “An Efficient Energy Management Approach for a Solar-Powered EV Battery Charging Facility to Support Distribution Grids,” *IEEE Transactions on Industry Applications*, vol. 55, no. 6, pp. 6517-6526, 2019. [CrossRef] [Google Scholar] [Publisher Link]

[31] Rajesh Kumar Lenka et al., “PV Integrated Multifunctional Off-Board EV Charger with Improved Grid Power Quality,” *IEEE Transactions on Industry Applications*, vol. 58, no. 5, pp. 5520-5532, 2022. [CrossRef] [Google Scholar] [Publisher Link]

[32] Vandana Jain, Bhim Singh, and Seema, “A Grid Connected PV Array and Battery Energy Storage Interfaced EV Charging Station,” *IEEE Transactions on Transportation Electrification*, vol. 9, no. 3, pp. 3723-3730, 2023. [CrossRef] [Google Scholar] [Publisher Link]

[33] Nishant Kumar et al., “Power Quality Improved Grid-Interfaced PV-Assisted Onboard EV Charging Infrastructure for Smart Households Consumers,” *IEEE Transactions on Consumer Electronics*, vol. 69, no. 4, pp. 1091-1100, 2023. [CrossRef] [Google Scholar] [Publisher Link]

[34] G.R. Chandra Mouli, P. Bauer, M. Zeman, “System Design for a Solar Powered Electric Vehicle Charging Station for Workplaces,” *Applied Energy*, vol. 168, pp. 434-443, 2016. [CrossRef] [Google Scholar] [Publisher Link]

[35] K. Kanimozhi et al., “Design and Laboratory Validation of a Grid-Interfaced Totem-Pole PFC Converter with PR Controller and Isolated Phase Modulated Converter for Solar-Powered Next-Gen EV Charging System,” *CPSS Transactions on Power Electronics and Applications*, vol. 10, no. 1, pp. 32-43, 2025. [CrossRef] [Google Scholar] [Publisher Link]

[36] Bo Yang et al., “PV Arrays Reconfiguration for Partial Shading Mitigation: Recent Advances, Challenges and Perspectives,” *Energy Conversion and Management*, vol. 247, 2021. [CrossRef] [Google Scholar] [Publisher Link]

[37] Arumugam Manthiram, “A Reflection on Lithium-Ion Battery Cathode Chemistry,” *Nature Communications*, vol. 11, no. 1, pp. 1-9, 2020. [CrossRef] [Google Scholar] [Publisher Link]

[38] Bharath Pattipati et al., “Open Circuit Voltage Characterization of Lithium-Ion Batteries,” *Journal of Power Sources*, vol. 269, pp. 317-333, 2014. [CrossRef] [Google Scholar] [Publisher Link]